Supplement of Atmos. Meas. Tech., 15, 3481–3495, 2022
https://doi.org/10.5194/amt-15-3481-2022-supplement
© Author(s) 2022. CC BY 4.0 License.

Atmospheric Measurement Techniques
Open Access

Supplement of

Impact of 3D cloud structures on the atmospheric trace gas products from UV–Vis sounders – Part 3: Bias estimate using synthetic and observational data

Arve Kylling et al.

Correspondence to: Arve Kylling (arve.kylling@nilu.no)

The copyright of individual parts of the supplement might differ from the article licence.

S1 Summary of LEO and GEO cases

To summarize the overall differences between the retrieved and true NO_2 TVCDs for all synthetic LEO and GEO cases, the number n of pixels with differences d: $d < -20; -20 < d < 20; -10 < d < -10; d > 20\%$ were calculated (Fig. S1.) For the GEO geometry, between 87.6±0.6% (solar zenith angle, SZA=20°) and 64±2.5% (SZA=60°) of the retrieved NO_2 TVCD are within ±10% of the "true" column for an albedo of 0.0 (black solid lines, Fig. S1a). These numbers decrease by about 8-10% points for larger surface albedos of 0.05 to 0.2 (dotted and dashed lines). The number of pixels within ±20% decrease from 98.8±0.4 to 79.4±2.4 as the SZA increase from 20° to 60° for an albedo of 0.0 (green solid lines, Fig. S1a). The number of pixels with differences $< -20\%$ increase from about 1.0% for low albedo and SZA=20° to up to 17% for high albedo and SZA=60° (red lines Fig. S1a). The number of pixels with differences $> 20\%$ is zero for SZA=20° and never above 3.3% for other SZA. The overall bias is -0.9%. The variation with solar azimuth angle is small for SZA=20° and SZA=40°, but increase for SZA=60°. The viewing angles are constant for the GEO cases and thus no variations are seen.

For the LEO geometry between 82.6±3.3% (SZA=20°) and 58.9±2.1% (SZA=60°) of the retrieved NO_2 TVCDs are within ±10% of the true column for an albedo of 0.0 (black solid lines, Fig. S1b). These numbers decrease by about 7% points for larger surface albedos. The number of pixels with differences within ±20% decrease from 97.0±3.1 to 76.3±3.5% as the SZA increases from 20° to 60° for an albedo of 0.0 (black solid lines, Fig. S1b). The number of pixels with differences $< -20\%$ increase from about 2.6±2.7% for low albedo (0.0) and high sun (SZA=20°) to up to 22.4±2.4% for high albedo (0.2) and low sun (SZA=60°, solid and dashed red lines, Fig. S1b). The number of differences $> 20\%$ are below 3.9% for all cases (blue lines, Fig. S1b). The bias is -0.5%. The differences shows no strong dependence on the viewing azimuth angle. However, the number of points within ±10% decrease by 4-8% for large viewing angles (VZA=60°) and SZA<= 40° (black lines, Fig. S1b).

S2 Cloud shadow band cases

Based on the findings from the analysis of the synthetic data we searched TROPOMI and VIIRS data for cases with cloud shadows and large solar zenith angles. An example of a cloud shadow band is shown in Fig. S2 (pointed to by the red arrow in Fig. S2a). The NO_2 TVCD, Fig. S2b, is markedly higher in the Amsterdam area, but is otherwise overall slowly varying over the region. The H-metric, Fig. S2c, is sensitive to inhomogeneous clouds, but also to variations in the surface albedo, compare Fig. S2a and S2c. The geometric cloud fraction, based on the VIIRS cloud mask, shows larger variability than the average radiometric cloud fraction CF_r^{VIIRS}, as expected, compare Fig. S2d and S2e and see also the distributions of these quantities in Fig. S2h. The cloud shadow fraction, Fig. S2f, is between 0.2 and 0.5 in the area with scattered clouds. The cloud shadow fraction also clearly delineates the large cloud structures. The cloud shadow band has a width about the extent of 1-2 TROPOMI pixels. As the cloud shadow band and the TROPOMI pixels are not aligned this implies that the cloud shadow band at some locations will be completely covered by one TROPOMI pixel and at other locations partly covered by two TROPOMI pixels. This causes the oscillatory pattern seen in the geometric cloud fraction (Fig. S2d) and the cloud shadow fraction (Fig. S2f) in the cloud shadow band. The NO_2 TVCD versus the cloud shadow fraction is shown in Fig. S2g for all cloud shadow pixels. For a cloud shadow fraction < 0.5 the NO_2 TVCD decrease with increasing cloud shadow fraction. However, the decrease is well within the variability of the NO_2 TVCD (the red line with error bars indicates the average NO_2 TVCD ±standard deviation) and the scatter is too large to draw any conclusions about the dependence of the NO_2 TVCD on the cloud shadow fraction. The distribution of the H-metric for various CF_r^{VIIRS} is shown in Fig. S2i. For CF_r^{VIIRS} between 0.4 and 0.6 (green bars) maxima are found both for low (scattered clouds) and high (homogeneous clouds or surface) H-metrics indicating that the CF_r^{VIIRS} may not unambigiously be used to identify scattered cloud cases. For the absorbing aerosol index no obvious dependence between the AAI and the NO_2 TVCD is present for this region, see S3 for further details.

For the cloud shadow band pointed to by the red arrow in Fig. S2a, further analysis is provided in Fig. S3. A RGB zoom in of the cloud shadow band is shown in Fig. S3b where red marks indicate pixels with cloud shadow. The VIIRS cloud top height and the TROPOMI NO_2 TVCD are shown in Figs. S3c and S3d. The cloud top height, cloud optical thickness and the cloud fraction is shown for row 267 in Fig. S3e. The cloud shadow is just north of a cloud band with optical thickness up to 10 (slant optical thickness of about 15) and an altitude between 9-10 km. North of the cloud shadow band there are also some clouds at the same height but with a smaller optical thickness of around 1.5-2. These thinner clouds are not easily seen in the VIIRS RGB, Fig. S2a, but are present in the VIIRS cloud mask and thus the geometric cloud and averaged radiometric cloud fractions, Figs. S2d-e. The NO_2 TVCD for row 267 using FRESCO and OCRA/ROCINN cloud correction algorithms, is shown in Fig. S3f. The NO_2 TVCD inside the cloud shadow is low by about a factor $2-3$ compared with the NO_2 TVCD north of the cloud shadow. Fig. S3g displays the NO_2 TVCD south of the shadow, in the shadow and north of the shadow for rows 262-269 and the average of these. A shadow pixel is defined as having a CSF $> 50\%$ and $CF_w < 50\%$. For row 263 no pixels satisfied this criteria and therefore no data is shown in the shadow region for this row. Pixels to be included in the regions north and south of the shadow band (up to 4 TROPOMI pixels north and south of shadow band), where required to have CSF $< 25\%$ and $CF_w < 50\%$. Except for rows 262 and 269, the NO_2 TVCD is smaller in the cloud shadow band compared to the NO_2 TVCD north of the cloud shadow. The NO_2 spatial varibility is large (Fig. 12.d), despite this, for the cloud shadow band covered by rows 262-269, the NO_2 TVCD is on average reduced by 17%. There is no clear dependence of the NO_2 difference on the cloud shadow fraction. The cloud optical thickness of the cloud causing the cloud shadow varies little, the average cloud optical thickness being 9.0 ± 1.6. Thus it is not possible to say anything about the dependence of the NO_2 difference on the cloud optical thickness for this case.

Another example of a cloud shadow band and 3D cloud effects on NO_2 retrieval is shown in Fig. S4. The VIIRS RGB image (Fig. S4a) shows the cloud coverage over Northern Germany on December 30, 2019, when the solar zenith angle during the VIIRS and TROPOMI overpass time is larger than 70°. The cloud shadow is just north of a large cloud band, and most of the northern region is completely cloudless, which is similar to the idealized box cloud cases presented by Emde et al. (2022) and Yu et al. (2021). The cloud height from west to east is 1 km to 8 km (Fig. S4c). The cloud optical thickness is not available for this case, but from the RGB the cloud is clearly optically thick enough to make the ground not visible from space. To look for cloud shadow effects, we select the region within the red box in Fig. S4a. In Fig. S4e is shown the VIIRS reflectance and cloud top height for TROPOMI row 394 as a function of latitude. The pixels are identified as cloudy, cloud shadow and clear based on the reflectance; with the reflectance being about 0.25 over the clear region, down to 0.18-0.24 in the cloud shadow, and higher than 0.25 for cloudy pixels. There are four TROPOMI pixels in the cloud shadow where the NO_2 TVCD is low by 20-60% compared with the NO_2 TVCD to the north and south of the cloud shadow (cloud and clear pixels). There is a slight difference in the NO_2 retrieval using different cloud corrections, Fig. S4f. In order to reduce the influence of the signal to noise ratio, the NO_2 TVCD is averaged over cloudless (four pixels near the cloud shadow), cloud shadow and cloudy pixels (four pixel near the cloud shadow) for rows 393 to 398, as shown in Fig. S4g. For the cloudy pixels, the difference is within 10% between NO_2 averaged over all the pixels and NO_2 averaged for the pixels with high quality retrieval ($CF_w < 50\%$). With the exception of the cloudy pixels south of the cloud band for row 396, all other cases show that the NO_2 TVCD in the cloud shadow is lower by 8-46% (average of 25%) compared with the NO_2 TVCD around the shadow. Here, the NO_2 TVCD around the shadow represents NO_2 retrieval unaffected by 3D cloud, which is an average of NO_2 over cloudy and cloudless pixels, in order to reduce the impact of spatial variation of NO_2.

The time difference between the VIIRS and TROPOMI overpasses is about 4.2 min for the two cloud shadow band cases. For fast moving clouds this may give a shift in cloud and cloud shadow locations. For the two cloud band shadow cases discussed we investigated both ERA5 wind data and Spinning Enhanced Visible and InfraRed Imager (SEVIRI) RGB images. The SEVIRI images have a time resolution of 15 minutes and clearly show a southward movement of the cloud bands. The spatial resolution of SEVIRI together with possible cloud development make it challenging to precisely determine the speed of the cloud movement. We, however, estimate it to be on the order of 10-15 m/s in the southward direction perpendicular to the cloud shadow band. The ERA5 data have a large eastward component at the altitudes of the two cloud bands. For the 30 December 2019 case there is a much smaller southward component of about 10 m/s in agreement with the SEVIRI images. Surprisingly, for the 24 March 2019 case, the ERA5 data have a northward component of about 10 m/s, which is in disagreement with the SEVIRI observations. Trusting the SEVIRI images we find that the cloud mask and cloud shadow mask have shifted between 2.5 and 3.75 km perpendicular to the cloud shadow band between the TROPOMI and VIIRS overpasses. This is about the TROPOMI pixel size in this direction. For the 24 March 2019 case the cloud shadow band covers 1-2 TROPOMI pixels and it covers 2-4 TROPOMI pixels for the 30 December 2019 case. The cloud shadow band first viewed by VIIRS may thus be shifted southward when TROPOMI passes over. For the same geolocation, TROPOMI may thus view a smaller part of the cloud shadow band than VIIRS and hence cloud shadow affected TROPOMI pixels may be marked as not being affected by cloud shadow by VIIRS. In Figs. S3 and S4 we average over the TROPOMI pixels identified to be affected by cloud shadow according to the VIIRS cloud shadow mask. Despite a possible reduction in the cloud shadow viewed by TROPOMI, a decrease is seen in the NO_2 TVCD for these pixels. We note that the cloud shift may in principle be corrected for using for example ERA5 data. However, as reported above, we find that SEVIRI and ERA5 data give different results with respect to cloud movement.

If it is assumed that the clouds are the main reason for the variations in the NO_2 TVCD over the cloud shadow bands, then these cases are examples of how cloud shadows give underestimates of NO_2 TVCD, in agreement with the theoretical idealized box cloud results presented by Emde et al. (2022) and Yu et al. (2021).

S3 Absorbing aerosol index and NO_2 TVCD

Recently Kooreman et al. (2020) identified and explained absorbing aerosol index (AAI) large scale effects such as the cloud bow, sunglint and viewing zenith angle dependence. In addition they reported small-scale negative AAI values in partly cloudy areas and attributed this to 3D cloud structures casting shadow, but left the in-depth analysis for a future study.

As cloud shadow impact both AAI and NO_2 TVCD retrievals it is of interest to investigate possible relationships between the AAI and the cloud shadow fraction and the NO_2 TVCD. For the partly cloudy scene in Fig. S2, the TROPOMI AAI from 380 and 340 nm is shown in Fig. S5a. Overall the AAI is negative indicating the absence of absorbing aerosol, but the presence of scattering particles. The behaviour of clouds on AAI is complex. For effective cloud fraction between 30-50% (5-30%) for thick (thin) clouds Penning de Vries et al. (2009) reported negative AAI while for large cloud fractions high, thick clouds may cause positive AAI. The increase in AAI from scattered clouds to complete cloud cover may be seen when comparing Fig. S2d and Fig. S5a. For pixels with cloud shadows, the AAI does not vary with the cloud shadow fraction as shown in Fig. S5b. It is noted that the NO_2 TVCD varies considerably for these pixels, Fig. S5c. Thus, there appears to be no obvious dependence between the AAI and the NO_2 TVCD.

References

Emde, C., Yu, H., Kylling, A., van Roozendael, M., Stebel, K., Veihelmann, B., and Mayer, B.: Impact of 3D cloud structures on the atmospheric trace gas products from UV–Vis sounders – Part 1: Synthetic dataset for validation of trace gas retrieval algorithms, Atmospheric Measurement Techniques, 15, 1587–1608, https://doi.org/10.5194/amt-15-1587-2022, URL `https://amt.copernicus.org/articles/15/1587/2022/`, 2022.

Kooreman, M. L., Stammes, P., Trees, V., Sneep, M., Tilstra, L. G., de Graaf, M., Stein Zweers, D. C., Wang, P., Tuinder, O. N. E., and Veefkind, J. P.: Effects of clouds on the UV Absorbing Aerosol Index from TROPOMI, Atmospheric Measurement Techniques Discussions, 2020, 1–31, https://doi.org/10.5194/amt-2020-112, URL `https://www.atmos-meas-tech-discuss.net/amt-2020-112/`, 2020.

Penning de Vries, M. J. M., Beirle, S., and Wagner, T.: UV Aerosol Indices from SCIAMACHY: introducing the SCattering Index (SCI), Atmospheric Chemistry and Physics, 9, 9555–9567, https://doi.org/10.5194/acp-9-9555-2009, URL `https://acp.copernicus.org/articles/9/9555/2009/`, 2009.

Yu, H., Emde, C., Kylling, A., Veihelmann, B., Mayer, B., Stebel, K., and van Roozendael, M.: Impact of 3D Cloud Structures on the Atmospheric Trace Gas Products from UV-VIS Sounders - Part II: impact on NO 2 retrieval and mitigation strategies, Atmospheric Measurement Techniques, submitted, 2021.

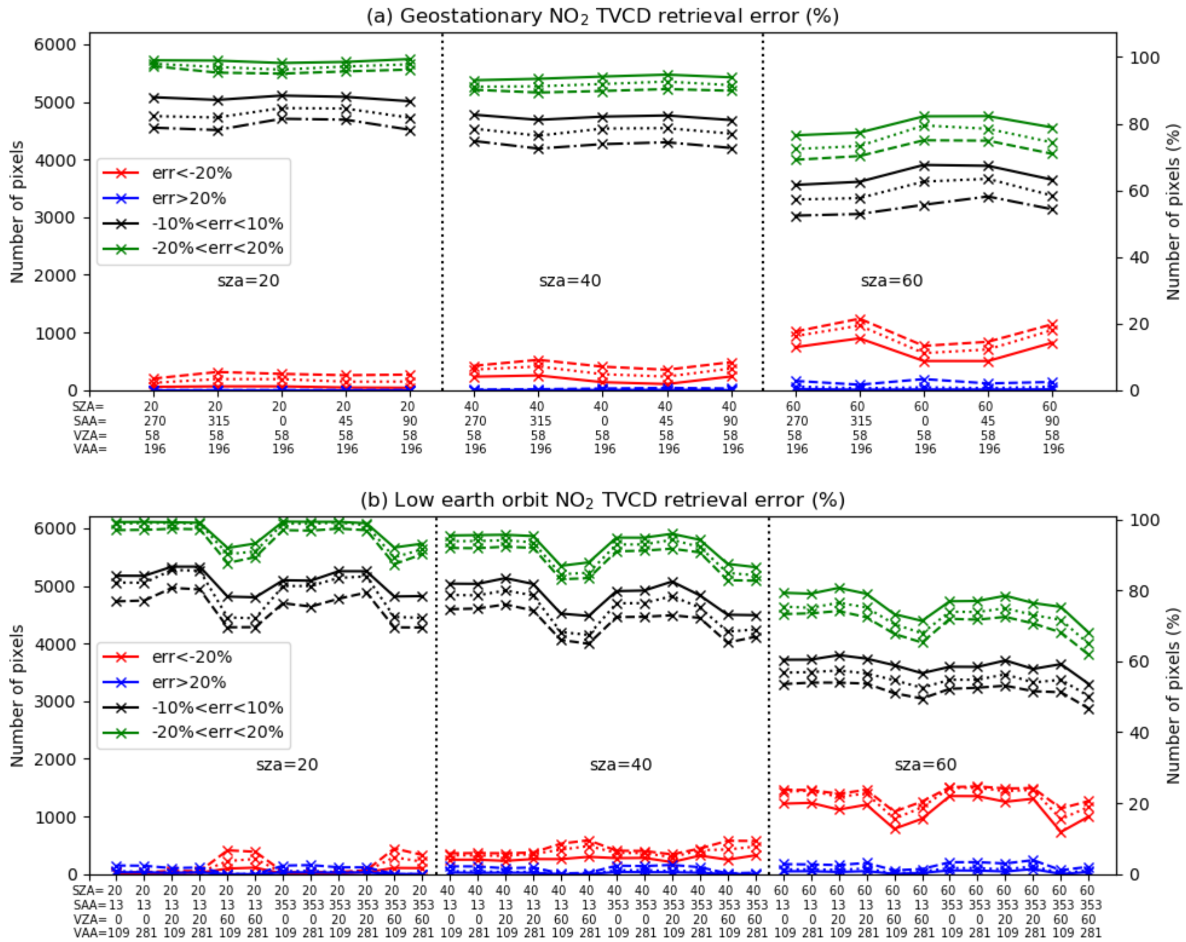

Figure S1: The number of pixels with NO_2 TVCD differences larger than 20% (blue lines) and less then -20% (red lines). The black and green lines are the number of pixels for which the differences are within ±10% and ±20%, respectively. Results are shown for geostationary (a) and low-earth-orbiting (b) geometries. The data points are connected by lines for increased readability, with solid lines being for an albedo of 0.0, dotted lines for 0.05, and dashed lines for an albedo of 0.2. The solar zenith (SZA) and azimuth angles (SAA) and the viewing zenith (VZA) and azimuth angles (VAA) are given on the x-axes. Note that the % is with respect to the total number of pixels for which a NO_2 retrieval has been done. This number is smaller than the number of pixels in the scene as cloud contaminated pixels are excluded from the retrieval.

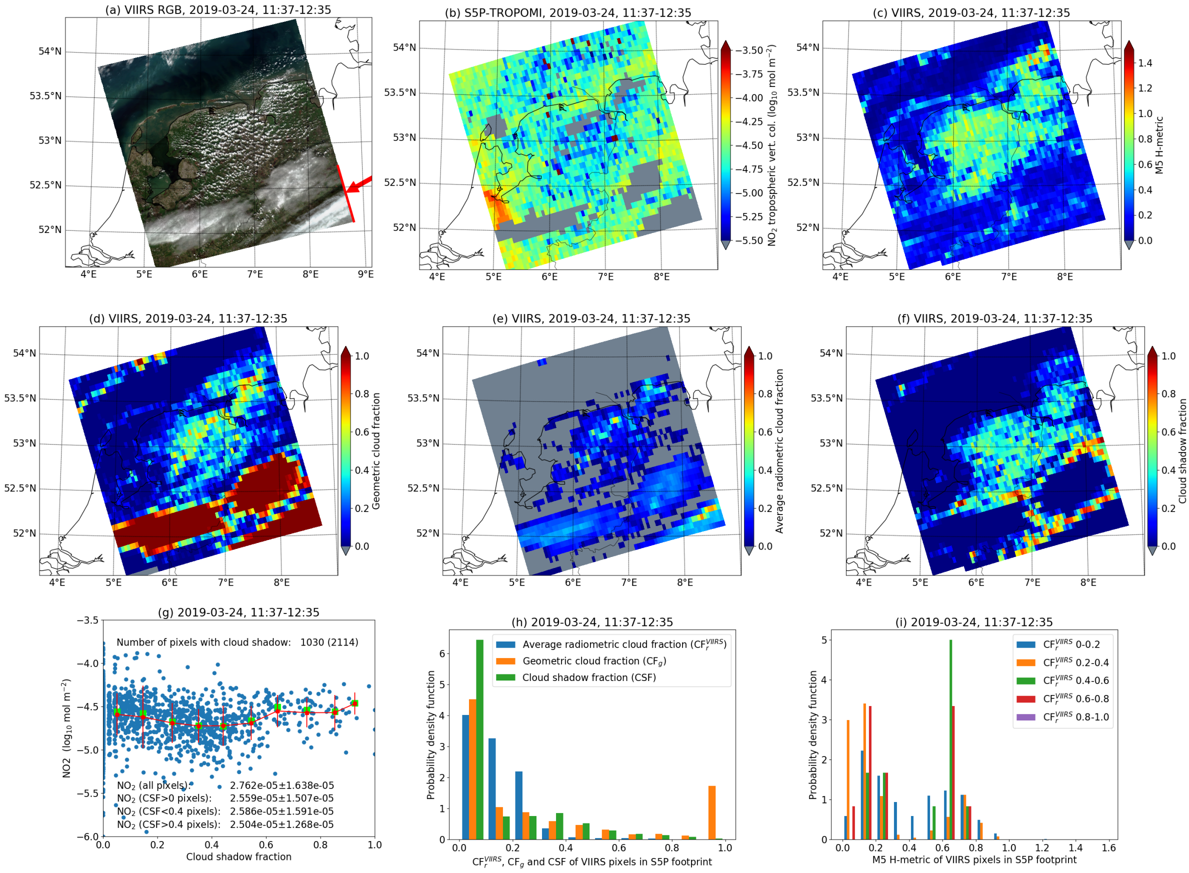

Figure S2: Examples of VIIRS and TROPOMI data and various CFMs for the cloud shadow band in Fig. 2. (a) VIIRS RGB. The red marked pixels correspond to the data shown in Fig. S3. (b) NO_2 TVCD from TROPOMI. (c) The H-metric from VIIRS band M5. (d) The cloud geometric fraction from VIIRS. (e) The cloud radiance fraction from VIIRS. (f) The cloud shadow fraction from VIIRS. (g) The NO_2 TVCD versus the cloud shadow fraction. The red lines is the average NO_2 TVCD with standard deviation (vertical lines). Lime green squares indicate the median NO_2 TVCD. (h) The distribution of the cloud radiance, cloud geometric and cloud shadow fractions. (i) The distribution of the H-metric for various cloud radiance fractions.

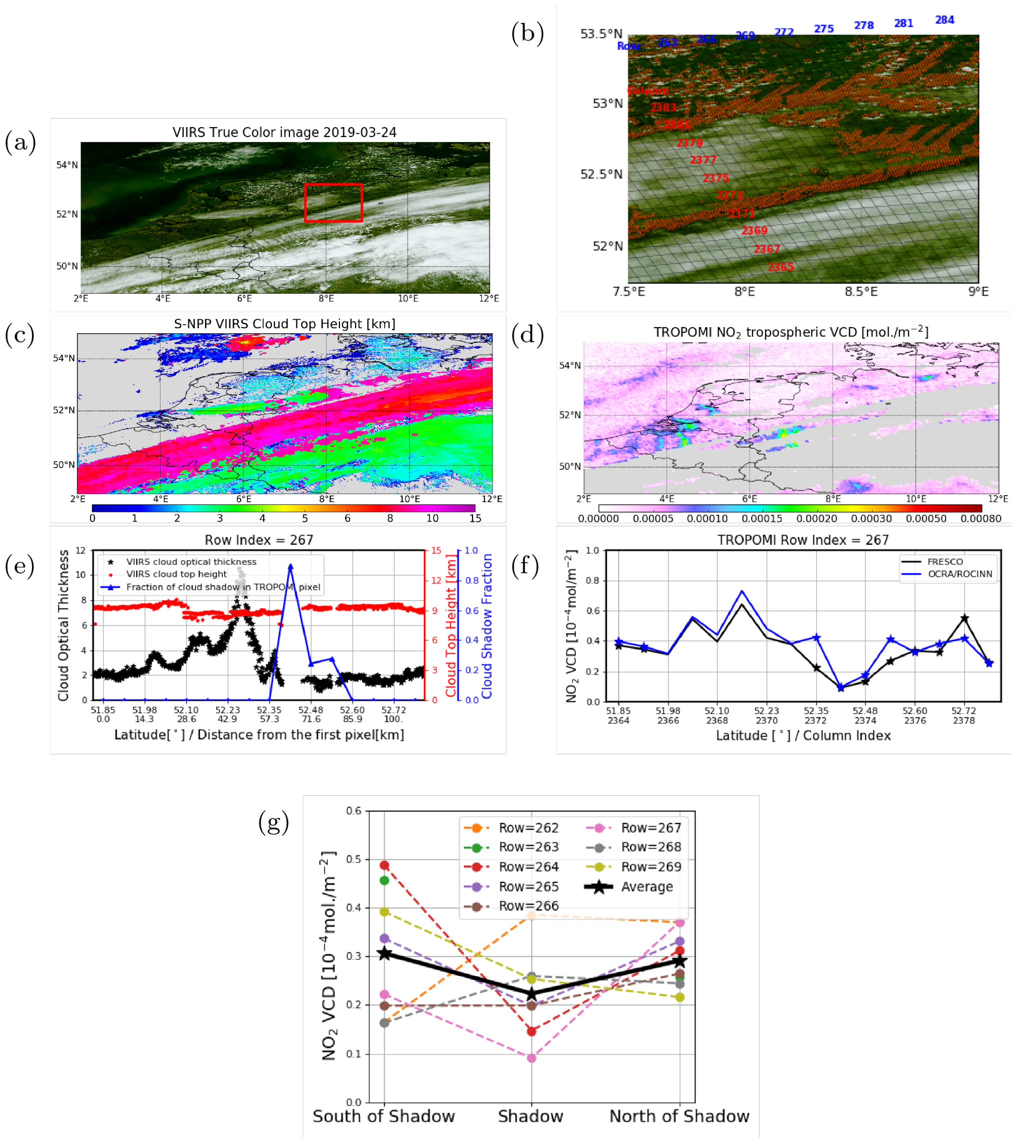

Figure S3: Another view of the cloud shadow band example in Fig. S2. (a) VIIRS RGB image; (b) zoom-in of cloud shadow band with TROPOMI footprint, red marks indicate pixels with cloud shadow; (c) the VIIRS cloud top height; (d) the TROPOMI NO_2 TVCD; (e) the VIIRS cloud optical thickness, cloud top height and cloud shadow fraction for TROPOMI row 267 (the row localisation is shown in panel b); (f) the NO_2 TVCD using FRESCO and OCRA/ROCINN cloud correction algorithms, as a function of latitude. The star marks represent pixels with $CF_w < 50\%$; (g) averaged NO_2 TVCD for pixels south of the shadow, in the shadow and north of the shadow for rows 262-269 and the average of these. See text for further details.

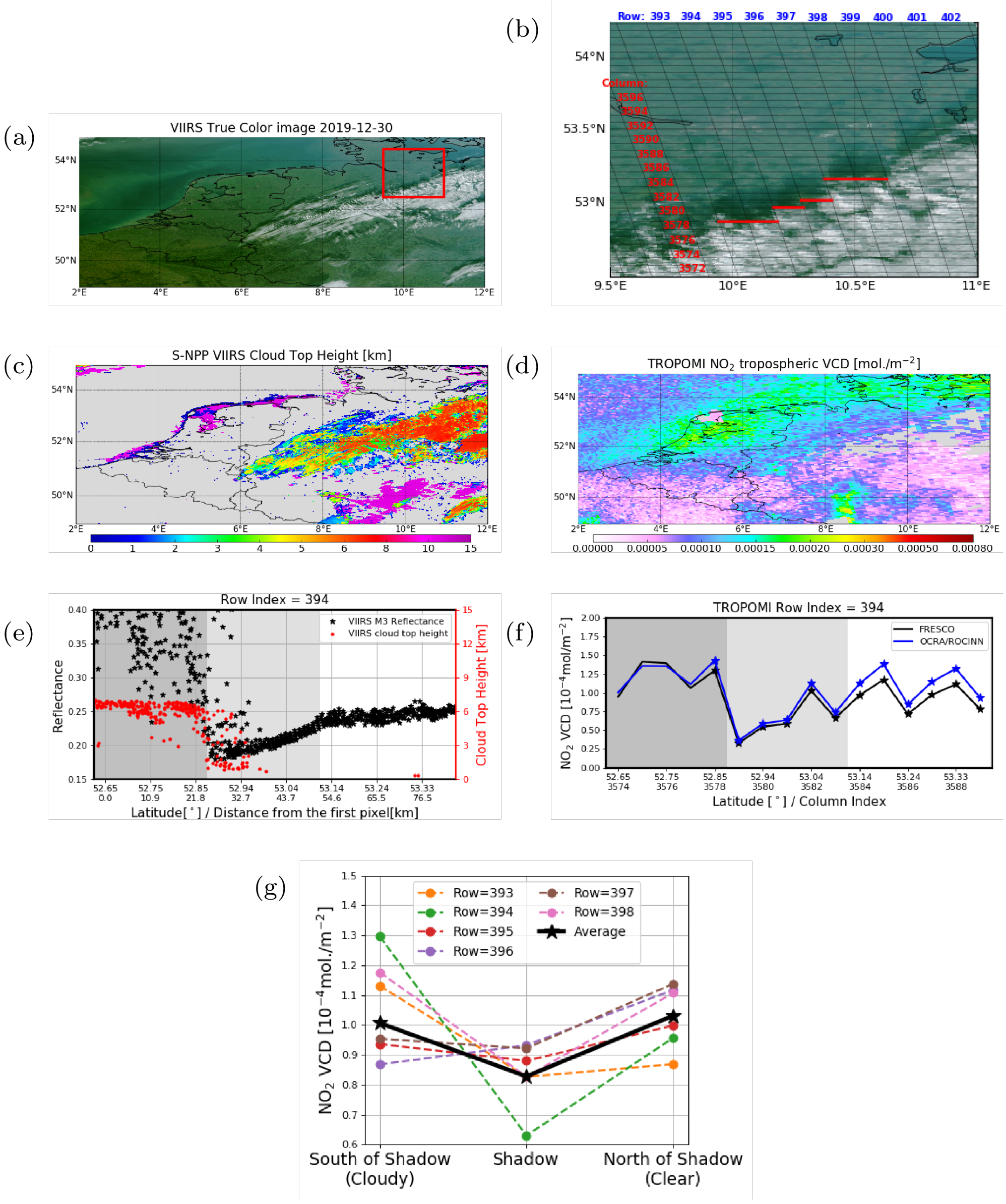

Figure S4: Similar to Fig. S3, but data for 30 December 2019. Furthermore, in (b) the red lines indicate the cloud edge in along-track direction for rows 393 to 398; in (e) no cloud shadow nor cloud optical thickness information is included, instead the VIIRS M3 reflectance is plotted; in (e)-(f) cloud, shadow and clear regions are identified as dark gray/light gray/white regions.

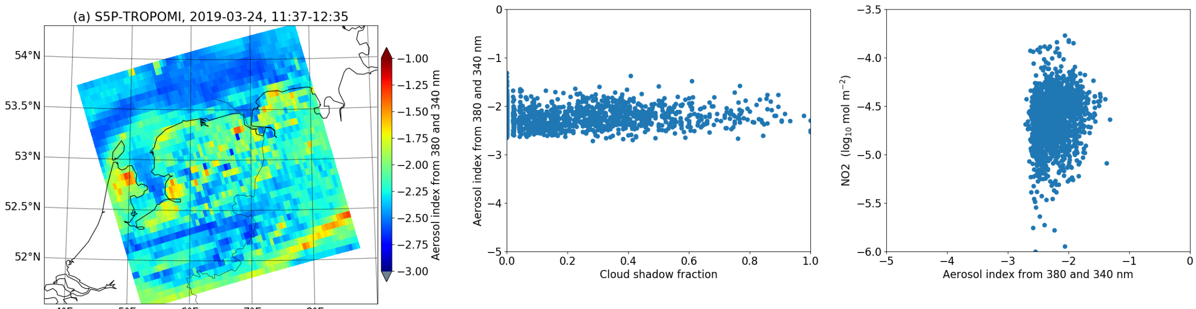

Figure S5: (a) The TROPOMI aerosol index. (b) The TROPOMI aerosol index versus the cloud shadow fraction. (c) The TROPOMI aerosol index versus the NO_2 TVCD. For (b) and (c) only data points where the NO_2 TVCD data quality flag > 0.95 and the AAI data quality flag > 0.5, are included. All data from 24 March 2019.